The 1995 November 22, M_w 7.2 Gulf of Elat earthquake cycle revisited

Gidon Baer,[1] Gareth J. Funning,[2]* Gadi Shamir[1] and Tim J. Wright[3]*

[1]*Geological Survey of Israel, 30 Malkhe Yisrael St., Jerusalem 95501, Israel. E-mail: baer@gsi.gov.il*
[2]*Department of Earth Sciences, University of California, Riverside, CA 92521, USA*
[3]*School of Earth and the Environment, University of Leeds, Leeds, UK*

SUMMARY

The 1995 November 22, $M_w = 7.2$ Nuweiba earthquake occurred along one of the left-stepping segments of the Dead Sea Transform (DST) in the Gulf of Elat (Aqaba). It was the largest earthquake along the DST in at least 160 yr. The main shock was preceded by earthquake swarms north and south of its NE-striking rupture since the early 1980s, and was followed by about 6 months of intense aftershock activity, concentrated mainly northwest and southeast of the main rupture. In this study we re-analyse ERS-1 and ERS-2 InSAR data for the period spanning the main shock and 5 post-seismic years. Because the entire rupture was under the Gulf water, surface observations related to the earthquake are limited to distances greater than 5 km away from the rupture zone. Coseismic interferograms were produced for the earthquake +1 week, +4 months and +6 months. Non-linear inversions were carried out for fault geometry and linear inversions were made for slip distribution using an ascending–descending 2-frame data set. The moment calculated from our best-fitting model is in agreement with the seismological moment, but trade-offs exist among several fault parameters. The present model upgrades previous InSAR models of the Nuweiba earthquake, and differs from recent teleseismic waveform inversion results mainly in terms of slip magnitude and distribution.

The moment released by post-seismic deformation in the period of 6 months to 2 yr after the Nuweiba earthquake is about 15 per cent of the coseismic moment release. Our models suggest that this deformation can be represented by slip along the lower part of the coseismic rupture. Localised deformation along the Gulf shores NW of the main rupture in the first 6 months after the earthquake is correlated with surface displacements along active Gulf-parallel normal faults and possibly with shallow $M > 3.9$, $D < 6$ km aftershocks. The geodetic moment calculated by modelling this deformation is more than an order of magnitude larger than expected for a single $M \sim 4$ aftershock, but could be a result of a sequence of aftershocks and/or aseismic slip. The major aftershocks and the slip along Gulf-parallel normal faulting NW of the main rupture are associated with positive Coulomb stress changes induced by the main event.

Key words: Seismic cycle; Radar interferometry; Earthquake dynamics; Earthquake source observations.

1 INTRODUCTION

The 1995 November 22 $M_w = 7.2$ Nuweiba earthquake was the largest seismic event along the Dead Sea Transform (DST) in at least 160 yr. The earthquake ruptured under the waters of the Gulf of Elat (Aqaba) along the Aragonese segment of the left-stepping DST (Fig. 1). In the absence of direct slip observations and GPS measurements along and in the vicinity of the rupture area, sur-

face deformation associated with the Nuweiba earthquake could be estimated only by interferometric synthetic aperture radar (In-SAR) observations (Baer *et al.* 1999, 2001; Klinger *et al.* 2000). The earthquake slip distribution was previously derived from inversion of teleseismic body-wave seismograms (Hoffstetter *et al.* 2003) and refined by integration of the seismological data with a 3-D mechanical model through comparison with the InSAR results (Shamir *et al.* 2003). Comparison between several previously published seismological solutions for the source parameters show significant differences (Shamir 1996; Pinar & Turkelli 1997; Klinger *et al.* 1999; Hoffstetter *et al.* 2003; Shamir *et al.* 2003). Previous InSAR studies
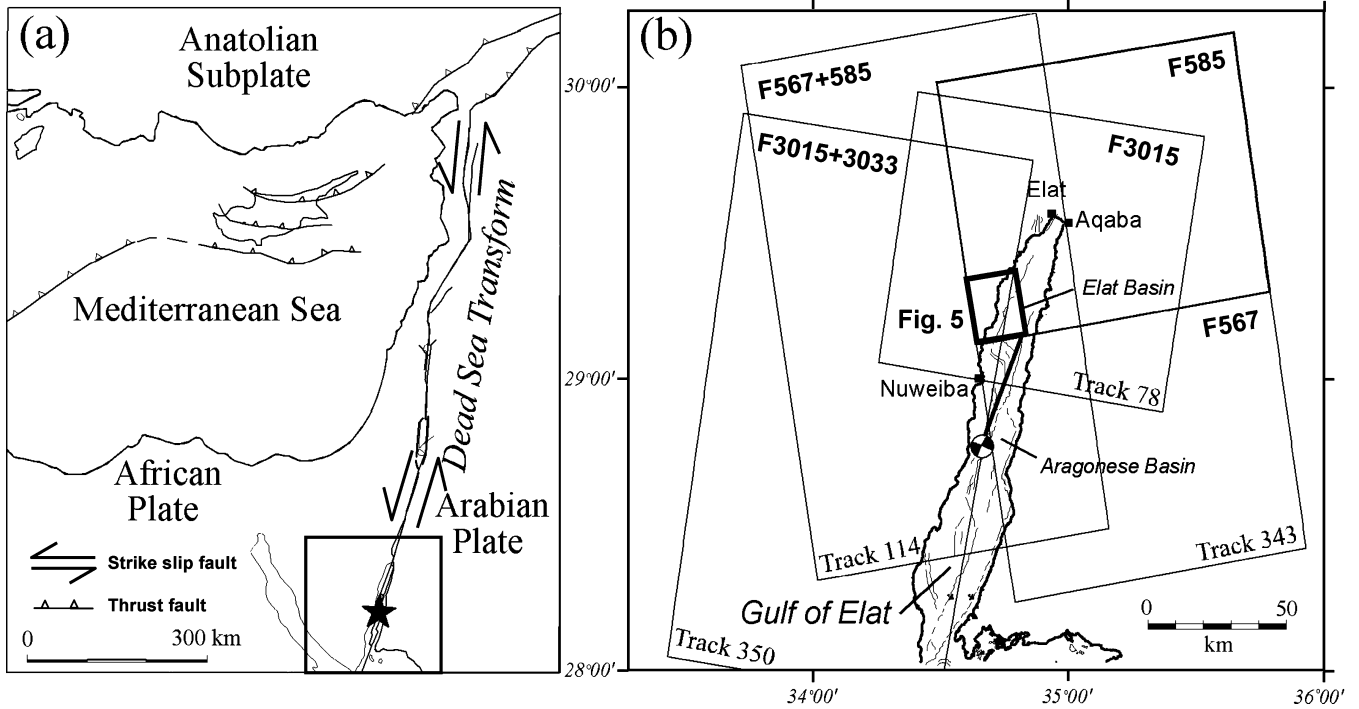
Figure 1. (a) General tectonic map (modified after Joffe & Garfunkel 1987) showing the major plates in the Levant and the Nuweiba earthquake (marked by star). (b) Map of the Gulf of Elat/Aqaba showing in grey the major faults (After Ben-Avraham 1985), the Nuweiba earthquake epicentre, and the inferred rupture (bold line). Also shown are the SAR frames (marked by F) and tracks selected for interferometry.

of this earthquake also yielded different fault models (Baer *et al.* 1999; Klinger *et al.* 2000; Shamir *et al.* 2003).

The Nuweiba earthquake was followed by intense aftershock activity, mainly during the first 6 months, with epicentres clustering mainly in the NW and SE quadrants relative to the main rupture (Hoffstetter *et al.* 2003). Post-seismic deformation imaged by InSAR was also found to concentrate NW of the rupture termination (Baer *et al.* 2001). Because of the use of partial SAR databases in all previous studies, the spatial coverage of both coseismic and post-seismic interferograms was incomplete, resulting in large ambiguities and trade-offs in the calculated fault models. The first objective of this study is thus to provide better constraints on the earthquake

source parameters by inversion of the displacement measurements using a significantly larger SAR data set than previously available.

Stress transfer and interaction have been shown to be fundamental properties of earthquakes (King *et al.* 1994; Toda *et al.* 1998; Stein 1999; King & Bowman 2003), and there is growing evidence that earthquakes trigger slip along favourably oriented faults and delay the slip on others (e.g. Bodin *et al.* 1994; Price & Sandwell 1998; Wright *et al.* 2001; Fialko *et al.* 2002; Amelung & Bell 2003). Changes in fault creep rate in the Arava Valley, the next DST segment to the north, also seemed to be temporally related to the Nuweiba earthquake (Sarti *et al.* 2003; Finzi 2005). For future seismic hazard evaluation of this region, we thus find it important to
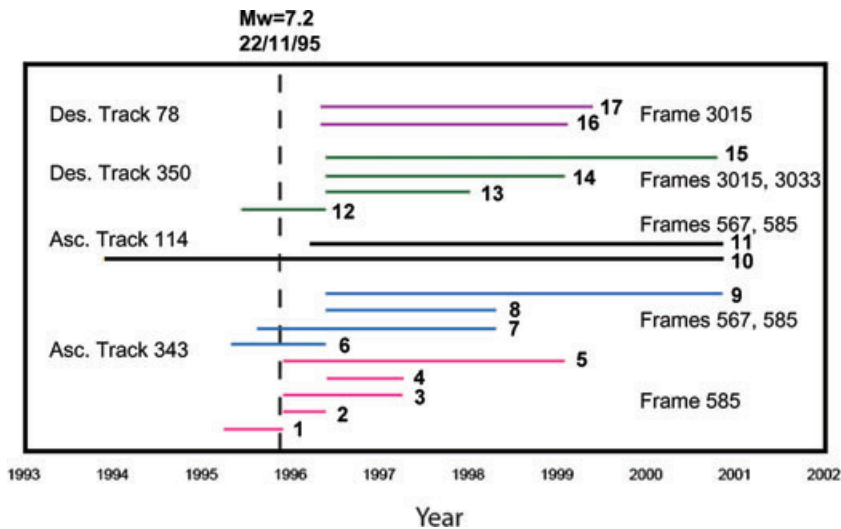
Figure 2. Acquisition times and interferometric pairs of scenes used in this study. Pairs 6, 8, 12 and 14 were inverted for fault parameters.

understand the relationships between the Nuweiba earthquake main shock, the post-seismic deformation and the aftershock sequences. In the second part of this study we evaluate the mechanisms of post-seismic strain release, calculate the Coulomb stress changes induced by the Nuweiba main shock and examine their effect on the occurrence of post-seismic deformation and major aftershocks.

2 INSAR PROCESSING AND RESULTS

In the last decade, SAR interferometry (InSAR) has become a widespread tool to measure subtle displacements at the ground surface (Gabriel *et al.* 1989; Massonnet & Feigl 1998; Bürgmann *et al.* 2000). It has been shown to be particularly effective for mapping displacement fields in the coseismic and post-seismic stages of the earthquake cycle. Given the scarcity of GPS data and the lack of surface observations for the Nuweiba earthquake (the entire rupture was submarine), InSAR observations provide the only non-seismological constraints on the source parameters of the earthquake (Baer *et al.* 1999, 2001; Klinger *et al.* 2000). For this study we used SAR data collected by the ERS-1 satellite, which imaged the area between 1993 January and 1996 May, and the ERS-2 satellite (1995 July to 2001 December). The SAR operates in C-band at a wavelength of 56.6 mm, with a normal orbital cycle of 35 days for each satellite. The deformation field is shown as interference (phase change) fringes, each fringe cycle corresponding to 28.3 mm of movement along the satellite line-of-sight (LOS) direction. We processed our data using the JPL/Caltech ROI-PAC software (Rosen *et al.* 2004). To remove the topographic phase from the phase changes due to ground displacements and to geocode the interferograms, we use the 3 arcsec Shuttle Radar Topographic Mission (SRTM) digital elevation model (DEM) (Farr & Kobrick 2000). The interferograms were unwrapped using the 'Branch-cut' algorithm which is part of the ROI-PAC software (Goldstein *et al.* 1988; Rosen *et al.* 2000). The zero point for unwrapping is by default at the centre of the interferogram, but it can be defined anywhere depending on the deformation and coherence in the interferogram.

We processed most of the available scenes acquired during the years 1993–2001 along two ascending (SSE–NNW) and two descending (NNE–SSW) satellite tracks (Figs 1 and 2), that cover the entire region surrounding the rupture zone. This significantly extends the previously analysed database (see Klinger *et al.* 2000; Baer *et al.* 2001). Two scenes of frame 585, track 343 were acquired shortly after the earthquake (7 and 8 days) (Figs 1 and 2) and enable time separation to a coseismic interferogram spanning the earthquake +1 week (pair 1; Fig. 2), and an early (1 week to 6 months) post-seismic interferogram (pair 2; Fig. 2). In the other frames, such separation cannot be made and the earliest post-seismic acquisition is about 5 months after the earthquake (pairs 6, 8, 9, 11–17; Fig. 2).

For the earthquake modelling we prefer to use a set of interferograms that span comparable time intervals and a wide spatial coverage around the rupture zone. We thus choose the coseismic earthquake +6 months interferograms (pairs 6 and 12) and the late post-seismic (6 months to ~3 yr) interferograms (pairs 8 and 14) rather than those in which the post-earthquake acquisition was closer in time to the earthquake (Frame 585; Fig. 1b, pair 1; Fig. 2), which are too far to the north, do not cover most of the rupture zone and include only a very small part of the deformation. Each image is composed of two consecutive scenes of 100 km × 100 km. Wrapped interferograms of the coseismic deformation are shown in Figs 3(a) and (b) and unwrapped coseismic and late post-seismic interferograms are shown in Figs 3(c)–(f). The arid conditions and the <100 m perpendicular baselines chosen, enable maintaining
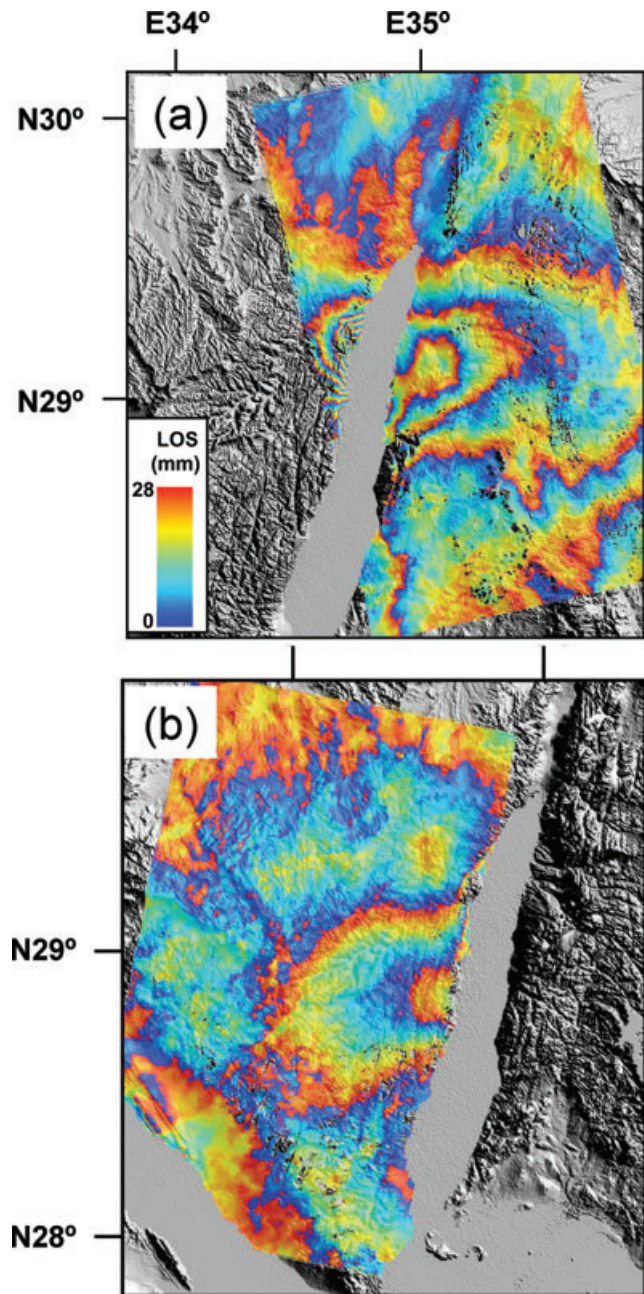
Figure 3. Coseismic and post-seismic interferograms of the Nuweiba earthquake. Each fringe cycle in the wrapped interferograms corresponds to 28.3 mm displacement in the satellite to ground line of sight (LOS). In the unwrapped interferograms, positive LOS displacement values indicate movement away from the satellite. (a) Wrapped, ascending track 343, coseismic interferogram for the period 1995 May 3–1996 May 23, with background map of the shaded relief SRTM digital elevation model. (b) Wrapped, descending track 350, coseismic interferogram for the period 1995 June 8– 1996 May 23. (c) Unwrapped interferogram of (a). (d) Unwrapped interferogram of (b). (e) Unwrapped, ascending track 343, post-seismic interferogram for the period 1996 May 22–1998 April 23. (f) Unwrapped, descending track 350, post-seismic interferogram for the period 1996 May 23—1999 January 29.

high coherence in most areas of the interferograms, except the Gulf waters. One may notice that the descending track coseismic interferograms (Figs 3b and d) show less changes than the ascending track interferograms (Figs 3a and c) because the descending track is
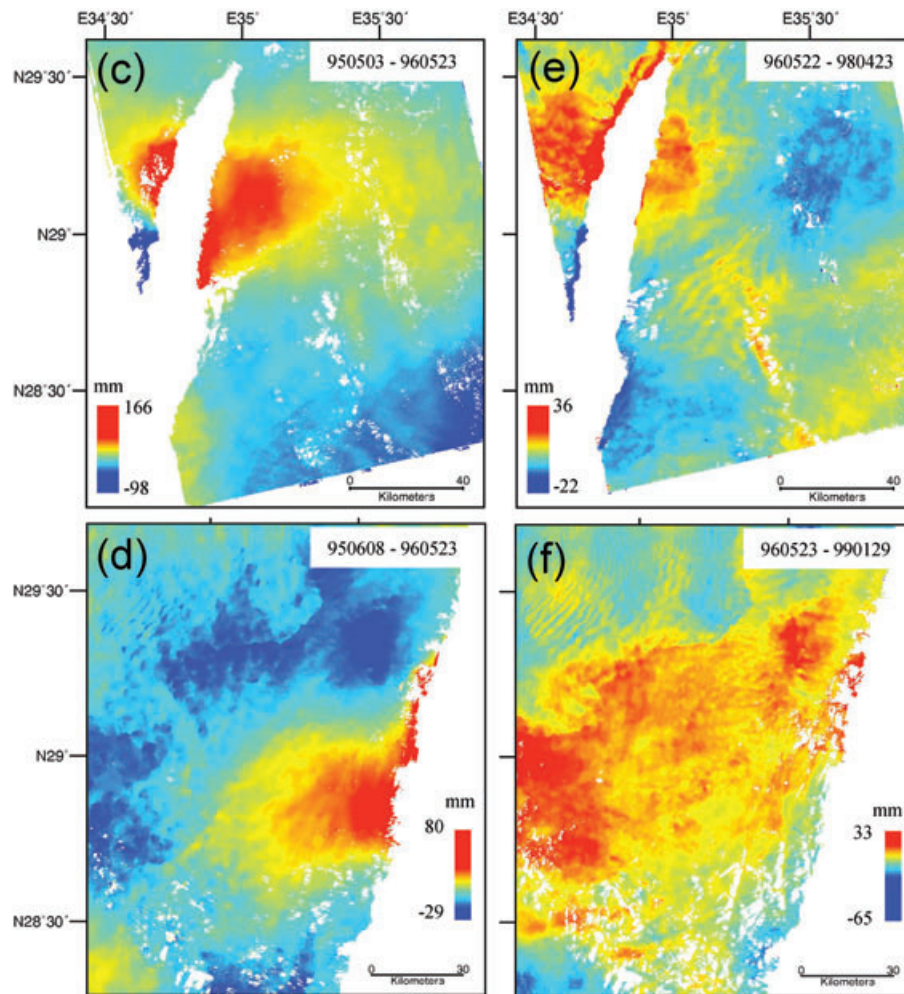
Figure 3. (*Continued.*)

almost parallel to the earthquake rupture, and thus the component of displacement in the satellite to ground direction is smaller in that interferogram. The general pattern of deformation in the late post-seismic interferograms (6 months to ∼3 yr) resembles the coseismic pattern, with about 15 per cent of its magnitude (Figs 3c–f).

For a better resolution of the early post-seismic period we generated four interferograms from frame 585 (Fig. 4): (1) Coseismic +1 week (pair 1; Fig. 2), (2) 1 week to 6 months after the earthquake (pair 2; Fig. 2), (3) 1 week to 17 months (pair 3; Fig. 2) and (4) 6–17 months after the earthquake (pair 4; Fig. 2). During the first 6 months deformation is concentrated in a 10 km × 10 km region located about 50 km SW of the tip of the Gulf (Figs 4b and c), where the large lobe of coseismic deformation was also observed (Figs 3a and 4a), and later than 6 months deformation occurs also at the eastern Gulf shoreline (Figs 3e and 4c, d). In the first 6 months two interferometric fringes that are truncated at their southern side by a NE-striking lineament are seen (Figs 5a and b). This lineament coincides with a fault line previously mapped in the Precambrian basement rocks (Fig. 6; see discussion below). The deformation in this particular region during the first week after the earthquake can also be resolved by subtracting an earthquake model (derived below) from an interferogram that spans the earthquake plus 1 week (Pair 1, Fig. 2). The residual interferogram (Fig. 5c) shows phase changes south of the line described above, however, the exact meaning of this signal is still unclear. The residual between the interferogram

that spans the earthquake plus 6 months and the earthquake model derived below (Fig. 5d) shows a pattern that resembles the 6 months post-seismic deformation (Fig. 5a).

3 COSEISMIC DEFORMATION ANALYSIS

3.1 Elastic dislocation modelling of InSAR measurements

Because of our choice of wide coverage rather than time proximity to the main shock, the coseismic interferograms used for inversion and modelling include deformation that occurred during the first 6 months after the earthquake, while the post-seismic interferograms cover only the time from 6 months after the earthquake onwards.

To obtain a set of fault parameters from the displacement observations we use the formulations of Okada (1985). These formulations show that for a finite dislocation, most static fault parameters except slip along the fault have non-linear relationships with the displacement field in the surrounding volume. The amount of slip and its distribution along the fault are linearly related to the displacements. Thus, we first solve the non-linear inverse problem and then invert the data linearly for the slip distribution. For the non-linear inversion we use an updated version of the *okinv* inversion program (Clarke *et al.* 1997; Wright *et al.* 1999) and for the linear inversion of the slip
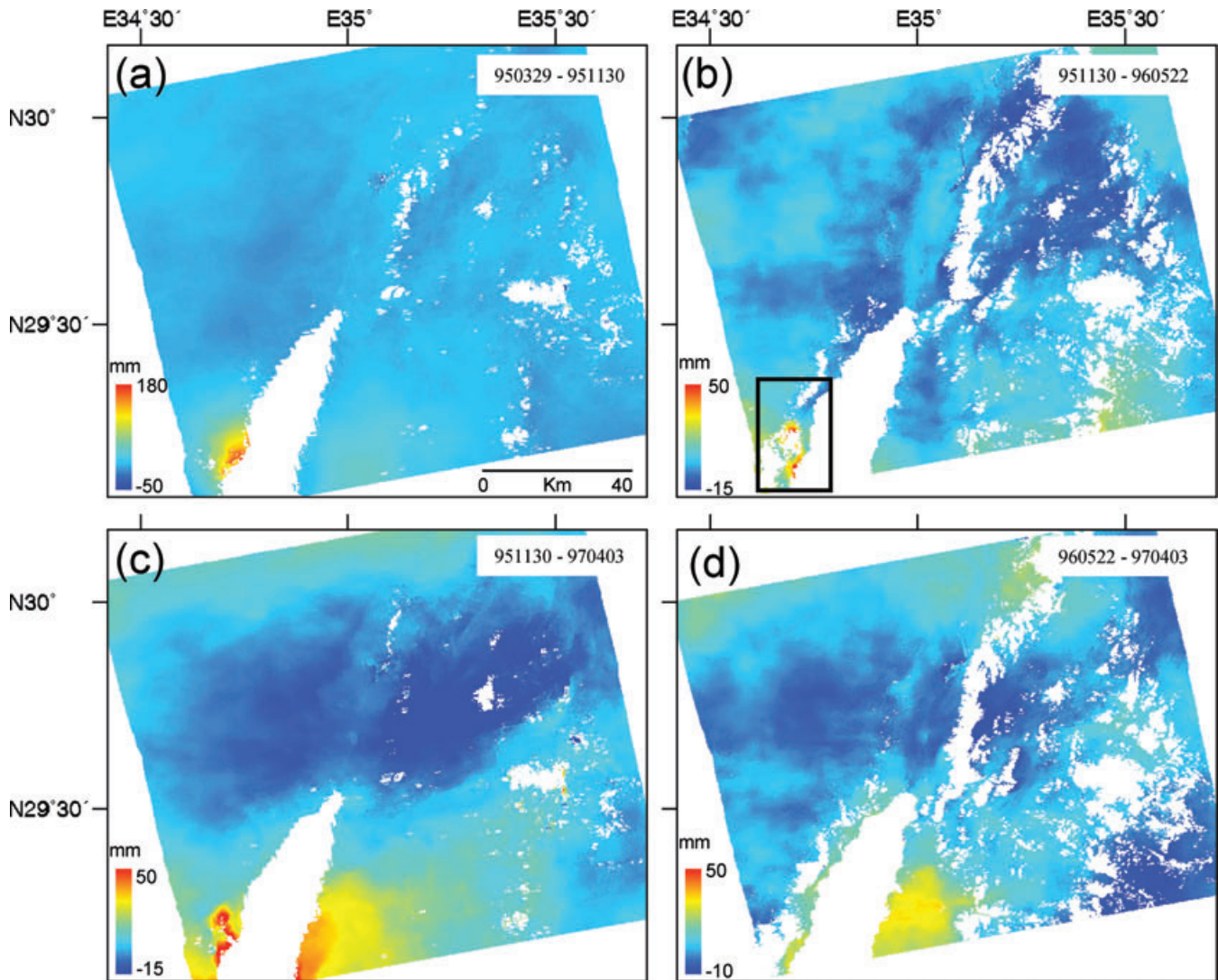
Figure 4. Frame 585 unwrapped interferograms showing temporal resolution that is unavailable in the 2-frame interferograms. (a) Coseismic +1 week. (b) Early post-seismic for the period 1995 November 30–1996 May 22. Black rectangle marks the area shown in Figs 5 and 6. (c) Post-seismic for the period 1995 November 30–1997 April 3. (d) Post-seismic for the period 1996 May 22–1997 April 3.

distribution we use the *slipinv* MATLAB coded program (Funning 2005). The algorithm used in *okinv* to manipulate the fault parameters until a minimum misfit is found is a Powell algorithm (as found in Press *et al.* 1992), and the variable slip modelling uses the Fast Non-Negative Least-Squares algorithm (Bro & De Jong 1997) to find a least-squares solution without the fault moving backwards.

Assuming the simple solution of a single fault with uniform slip we first search for a set of fault parameters coincident with a minimum misfit between modelled displacements, calculated using Okada's (1985) formulation, and the observed displacements. During the inversion all the static parameters (strike, dip, rake, location, length, top and bottom depths and slip) are free to vary around predetermined starting-values which were chosen from the most recent seismological solution of Shamir *et al.* (2003) (Table 1). We use two interferograms (ascending and descending orbits), resampled from ∼1.5 million points each to less than 1000 points each using a quadtree algorithm (e.g. Jónsson *et al.* 2002). The resampled data set is inverted with multiple (typically 100) random starting positions (Monte Carlo restarts). By using a range of starting positions

for the inversion, a range of minimum misfits can be calculated, with the smallest corresponding to the best-fitting set of model parameters. Comparison between the synthetic interferograms, calculated with the Okada (1985) formulation using these best-fitting fault parameters (Table 1), and the observed interferograms, yields 1–2 residual fringes along several sections of the Gulf shorelines. The rms misfit of the best-fitting uniform slip model to the InSAR data is 12.5 mm.

To determine the slip distribution along the fault we then discretize the fault into 5 km × 5 km patches, extend the fault length by 15 km on each end and fix all the parameters to the best-fitting non-linear solution. We then linearly invert the data for variable slip along the fault, and search for the best-fitting slip distribution. To avoid non-realistic oscillations in slip between adjacent patches we smooth the solution by minimizing the 2-D second derivative of the fault slip (for more details of the procedure, see Jónsson *et al.* 2002 and Funning *et al.* 2005). The residual phase between this model and the observed interferogram (Fig. 7) shows minor changes compared to the residual in the uniform slip model, and the rms misfit
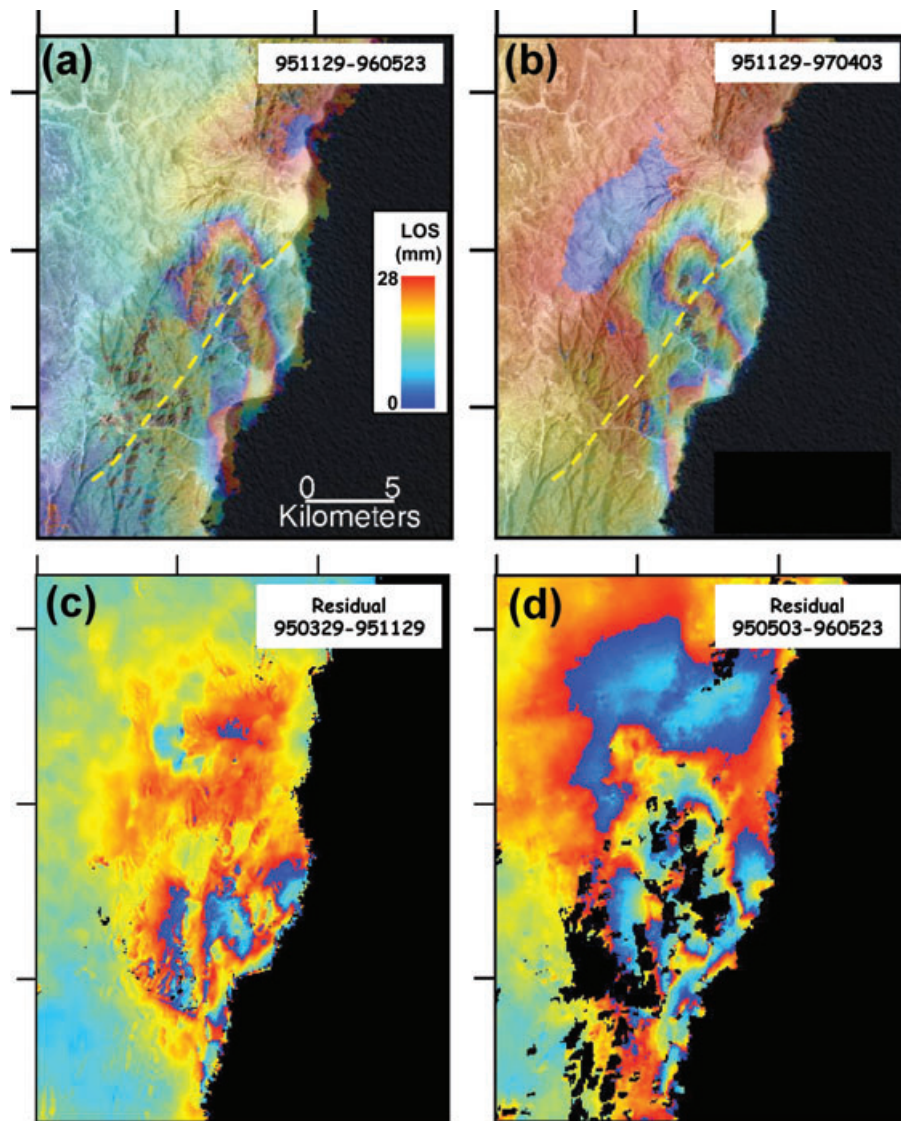
Figure 5. Early post-seismic wrapped interferograms of the area NW of the main rupture (black rectangle in Fig. 4b) for the period spanning (a) 1 week to 6 months after the earthquake. (b) 1 week to 17 months after the earthquake. (c) The residual phase in this area between the earthquake +1 week interferogram and the earthquake model derived below. (d) The residual phase between the earthquake +6 months interferogram and the earthquake model.

of the best-fitting variable slip model to the InSAR data is 11.5 mm. This marginal (<10 per cent) fit improvement reflects the masking of the near-field deformation (which is more affected by the slip distribution) by the Gulf waters and the low contribution of the slip details at 5–10 km distance from the fault. Most of this misfit is due to the first 6 months post-seismic deformation NW of the rupture termination (Figs 4 and 5) which is included in the coseismic inter-ferogram but is not included in the coseismic model. The 2–3 widely spaced fringes east of the southern rupture termination (Fig. 7b) could not be reproduced by slip along the fault or along additional fault segments and are thus probably due to the atmospheric effects (see below). The fault model (Fig. 7e) shows a zone about 30 km × 10 km in size at depth of 5–15 km with slip of 2–3 m, gradually decreasing to the surface, sideways and downdip. Since there is no additional data pertaining to the near field deformation, we consider this model satisfactory and find no need for further improvement by means such as additional fault segments or inversion for variable slip rake.

3.2. Error estimation

To estimate the uncertainties and trade-offs in our inverse models, we use a Monte Carlo technique in which we invert 100 perturbed data sets with noise characteristic to our data (see Funning *et al.* 2005). The altitudes of ambiguity of the two coseismic interfero-grams used in our inversion are 185 and 125 m, which are considerably higher than the ∼7 m accuracy of the SRTM DEM (Farr & Kobrick 2000), used to correct the topographic phase. We thus presume that the major source of noise in the data is not DEM errors but atmospheric conditions that delay the radar signal differently at the each acquisition time. We distinguish two major types of atmospheric signals (see Hanssen 2001, for a comprehensive overview): (1) A signal resulting from turbulent processes in the atmosphere, which adds to or subtracts from the phase changes in an irregular pattern (see central part of Fig. 3e, and northwestern part of Figs 3d and f). (2) A signal resulting from vertical stratification and different vertical refractivity profiles during the two SAR
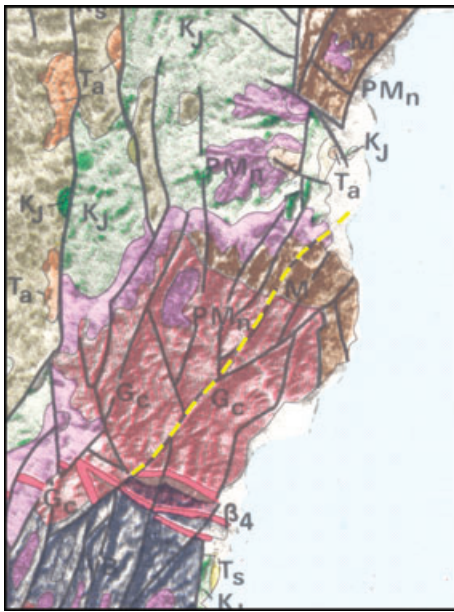
Figure 6. Geological map of the area NW of the main rupture showing the onshore fault lines (from Bartov *et al.* 1980). Yellow dashed line marks the location of the NE-striking lineament that truncates the interferometric fringes in Fig. 5. PMn – Cambrian to Cenomanian (undivided); Kj: Cenomanian–Turonian; Ta: Eocene; Ts: Oligocene–Miocene; β4: Miocene dykes.

acquisitions. This signal is generally correlated (or anticorrelated) with topography (see western parts of Figs 3d and f). The different evaporation conditions over the Gulf waters in the various SAR acquisitions may also contribute to the atmospheric phase delay and is superimposed on the two major signal sources (see for example, the northwestern Gulf shoreline in Fig. 3e, in which the phase delay is both topographically and shoreline- correlated). The atmospheric

effects are naturally more pronounced when the deformation signal is lower, as is the case in the late post-seismic interferograms (Figs 3e and f).

To estimate the error in our coseismic inversions, we generated a variance–covariance matrix for the noise in the interferograms by sampling undeformed areas of the interferograms. We then generated over 100 data sets perturbed by that noise, and inverted each data set separately, obtaining 100 different best-fitting solutions. Fault parameter trade-offs are assessed using scatterplots (Wright *et al.* 2003; Funning *et al.* 2005) in which each parameter is plotted against all the others in each inversion solutions of the perturbed data sets (Fig. 8a). The uncertainty in each fault parameter is shown by frequency histograms with 1σ uncertainty curves. Apparent uncertainties are small because of the high smoothing (the resolution is low). Had we chosen higher resolution solutions (low smoothing) we would end up with much larger uncertainties (e.g. Menke 1989). The slip uncertainties are underestimates as they were calculated for fixed fault geometry and no freedom was given at that stage to re-invert non-linearly for the fault geometry.

Because of the high coherence in regions >10 km away from the assumed rupture zone, parameters that mostly affect the size and the pattern of deformation in the intermediate and far fields (such as the strike, slip, rake and length of the fault) are relatively well constrained by the inversion results and do not differ in all solutions by more than a few per cent. On the other hand, because of the Gulf waters, the dip, which mostly affects the near-field deformation, shows a large scatter of values (from 55° to 80°), and the trade-offs between the dip and the other parameters are significantly higher. However, we note that, on the whole, the range of moments calculated by our fault parameters (6–8 × 10^26 Dyn-cm) is in relatively good agreement with the moment derived by waveform inversion of seismological data (7.7 × 10^26 Dyn-cm; Hoffstetter *et al.* 2003). In a similar manner, the perturbed data inversions also enable to calculate the accuracy of the variable slip model (Fig. 8b). One standard deviation from the mean of the slip values on each patch may be

**Table 1.** Source parameters of the Nuweiba earthquake determined by previous studies and this study.

References	Events	Lat[a]	Lon[a]	Depth[b]	Strike (°)	Dip (°)	Rake (°)	Length	Width	Slip (m)	Moment[c]
Seismology											
1	1	28.94	34.74	14	203	81	−7	50	NA	0–3.2 (v)	5.8
2	2	28.4	34.6	10	92	38	−58	20	NA	0.4	0.74
		28.5	34.7	15	288	82	−164	40	NA	0.9	3.4
											4.14 (T)
3	3	28.829	34.825	18.8	191.6	58.6	−21.2	27.4	NA	0.42	1.07
		29.042	34.777	18.65	199.3	74.3	−5.0	61.0	NA	2.5	5.40
		29.277	34.786	5.15	24.7	67.2	−8.5	25.6	NA	0.74	0.953
											7.42 (T)
4	2	NA	NA	15 ± 1	205 ± 5	60 ± 2	−20 ± 5	10	NA	0–1 (v)	0.6 ± 0.03
		28.97	34.75	10 ± 1	202 ± 5	77 ± 2	−15 ± 5	50	NA	0–4.5 (v)	7.1 ± 0.1
											7.7 (T)
InSAR + seismology											
5	1	28.96	34.73	15	197	80	−14	55	11	3	5.98
									13	2	4.29
							15	1.4	3.81	
6	1	28.93	34.78	12	195.15	65	−15.5	56	NA	2.1	4.65
7	1	28.975	34.77	13 ± 1	200	80	−12–−35	48	14	0–5 (v)	7.0
8	1	28.97	34.75	11.25	197.5	67	−4	58.5	30	0–3 (v)	6.5

Notes: Reference 1 : Kikuchi (1995) and Shamir (1996); 2: Pinar & Turkelli (1997); 3: Klinger *et al.* (1999); 4: Hoffstetter *et al.* (2003); 5: Baer *et al.* (1999, 2001); 6: Klinger *et al.* (2000); 7: Shamir *et al.* (2003) and 8: This study. (v): variable slip; (T): total; depth, length and width are in kilometres. NA: non available.
[a]Centre of fault trace.
[b]Defined differently in each of the previous studies; in this study—centroid depth (average depth weighted by the fault slip).
[c] × 10^26 Dyn-cm.
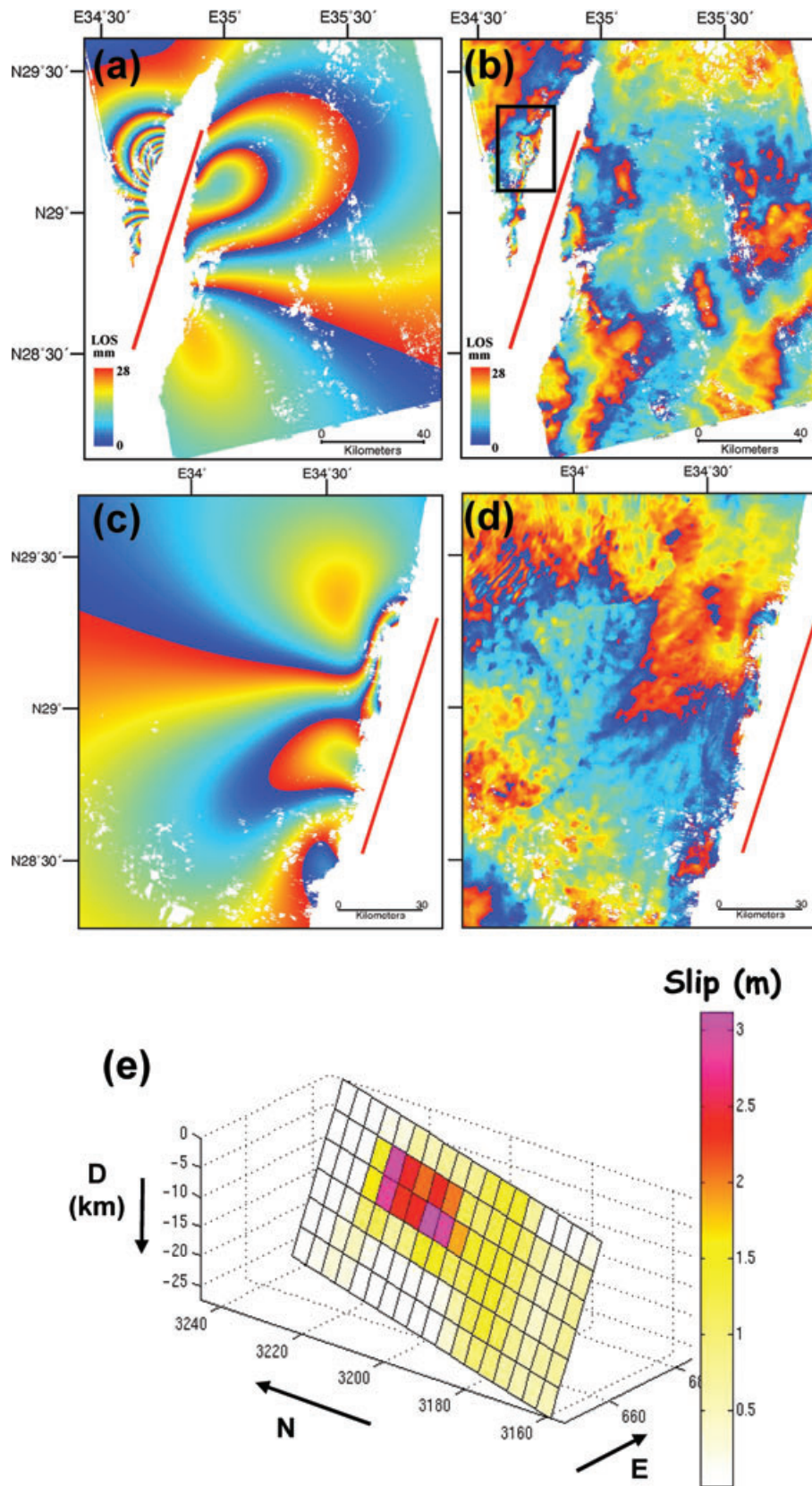
Figure 7. Best-fitting model interferograms (synthetic) and real-model residuals for the Nuweiba earthquake coseismic deformation, generated by non-linear inversion of the InSAR measurements (950503–960523 ascending and 950608–960523 descending interferograms), plus linear inversion for the slip distribution. Red lines mark the fault trace. (a) Ascending track model. (b) Ascending track residual. Black rectangle marks the residual also shown in Fig. 5(d). (c) Descending track model. (d) Descending track residual. (e) Slip distribution on the coseismic fault model.
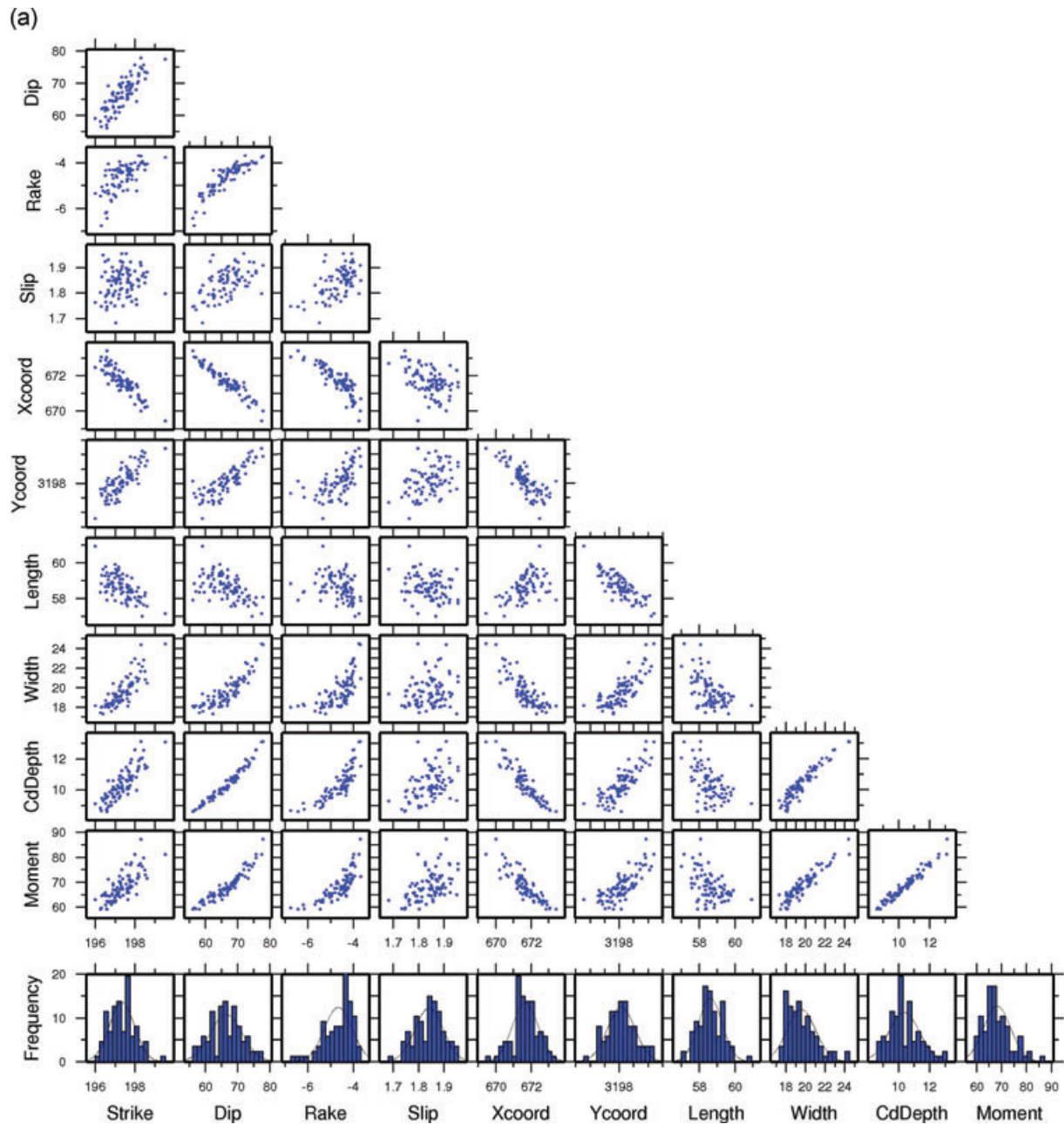
Figure 8. (a) Uncertainties and trade-offs of the model parameters computed using Monte Carlo analysis. Histograms show uncertainties in individual model parameters. Scatterplots show degrees of trade-off between pairs of model parameters in the inversion results of 100 perturbed data sets. Strike, dip and rake are in degrees; slip is in meters; *x* and *y* coordinates (of the centre of the fault plane projected up-dip to the surface) are in UTM km (zone 36); length, width and centroid (Cd) depth are in kilometers; moment is in units of 10^{25} Dyn-cm. (b) Plot of 1σ uncertainties in the slip values of the variable slip model (Fig. 7a), estimated using Monte Carlo analysis.

as high as 12 cm, indicating that the Gulf shorelines are far enough from the modelled rupture to be affected by small changes in the slip distribution.

4 POST-SEISMIC DEFORMATION ANALYSIS

4.1. Modelling of displacement data

Post-seismic fault parameters are obtained from the displacement observations of the late post-seismic period (6–29 months after the

main shock). The inversion procedure is similar to that described above for the coseismic deformation. Because of the low signal expected in the descending (fault-parallel) interferogram, we invert only the ascending 5/96–4/98 interferogram (Pair 8, Fig. 2). First, we carry out the non-linear inversion in which all the fault parameters are free to vary around pre-determined starting-values, and then perform a linear inversion for the slip distribution along the fault. The best-fitting solution of this inversion yields a fault that is located about 20 km east of the coseismic rupture, where no fault was mapped or suggested. We thus re-invert the data, fixing the strike, dip, rake and location of the fault to the coseismic
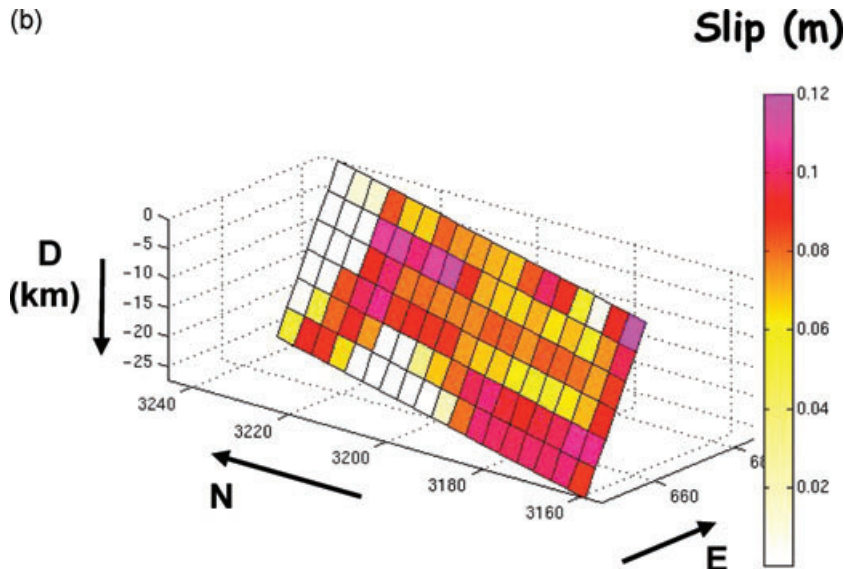
Figure 8. (*Continued.*)

parameters and solve only for the slip distribution, allowing the slipping patches to extend beyond the termination of the coseismic fault about 15 km along-strike and 10 km downdip. The rms misfit of this model (Fig. 9) to the InSAR data is about 5 mm. The higher residuals are mostly correlated to the topography or to the Gulf shoreline (Fig. 9b). Comparison between the coseismic and the post-seismic inversion results (Figs 7e and 9c) shows that while the main shock slip is concentrated at shallow depths (5–15 km), slip in the post-seismic stage seems to occur along deeper parts of the fault (20–30 km).

4.2. Triggered slip

An attempt to invert the early (1 week to 6 months) post-seismic observations (Figs 4b and c) for fault parameters yielded unrealistic results. The deformation is small and observed only at the edge of the interferogram on the two sides of the Gulf. Thus, we followed a forward modelling approach for the larger deformation lobe on the western coastline (Figs 4b and 5a). As model parameters we chose the location of the mapped lineament and the strike, dip and rake of the NW-dipping focal solution of aftershock #50 (Hoffstetter *et al.* 2003), the closest to the lineament termination (Figs 5a and 10a; Table 2). By trial and error we search for a simple slip distribution along the fault that best describes the observed deformation. Fig. 10(b) shows one of the possible solutions, a normal fault about 6 km long, divided into two patches slipping by 8 mm each and one patch slipping by 14 mm. The total moment calculated for the slip along this fault is 9.1×10^{23} Dyn-cm, which is consistent with an $M \sim 5.3$ earthquake, more than an order of magnitude higher than expected for the $M = 4.2$ earthquake. Given the relatively high uncertainty in aftershock locations in this region (due to poor station coverage) one cannot resolve unambiguously the spatial relations between the fault and the aftershocks. One possible scenario is that all the aftershocks occurred along the fault. In that case, the four aftershocks account for about 10 per cent of the geodetic moment. In a second scenario, the aftershocks are not concentrated along the fault, and under that assumption all the observed deformation may be due to aseismic slip along the NE-striking fault. A third possibility is that the aftershocks occurred on small asperities on

the fault plane loaded to failure by aseismic slip on the fault around them.

Next, we examine the possibility that induced stresses by the Nuweiba earthquake are the cause for the observed post-seismic deformation. Localised deformation along the Gulf shores NW of the main rupture was shown to correlate with surface displacements along Gulf-parallel normal faults and possibly with shallow $M > 3.9$, $D < 6$ km aftershocks during the first 6 months after the earthquake. In the absence of regional quantitative stress data, only changes in the shear (Coulomb) stress induced by the Nuweiba earthquake were calculated. The calculation used the Coulomb 2.5 algorithm (Toda & Stein 2002) and was based on the source parameters derived from the InSAR inversion model. The stress change distribution at 4 km depth, similar to the mean hypocentral depth of the four aftershocks analysed by Hofstetter *et al.* (2003), for the period between 1 week and 6 months after the main shock is shown in Fig. 11. These results suggest that the Nuweiba earthquake induced an increase in the Coulomb stress of 4–8 bars with respect to normal faulting on planes dipping 60° and striking 030–060° in the region of deformation NW of the main rupture (Fig. 11).

5 DISCUSSION

A major cause for discrepancy among this and previous studies of the Nuweiba earthquake is, obviously, the lack of near-field geodetic observations. In order to somewhat compensate for this inherent lacuna we processed a data set significantly larger than previously analysed. For each stage of the seismic cycle we chose pairs from different tracks that were temporally close to each other. This caused, on the one hand, a mixed coseismic and early post-seismic signal, but on the other hand, avoided the inversion of measurements related to different time intervals in different regions of the model, as occurred in most of the previous InSAR studies of this earthquake (Baer *et al.* 1999, 2001; Klinger *et al.* 2000). We therefore believe that the source parameters calculated here are more robust than in any of the previous studies. Because of this choice, the resulting coseismic model includes six post-seismic months and thus overestimates the coseismic deformation, while the post-seismic model underestimates the post-seismic deformation.
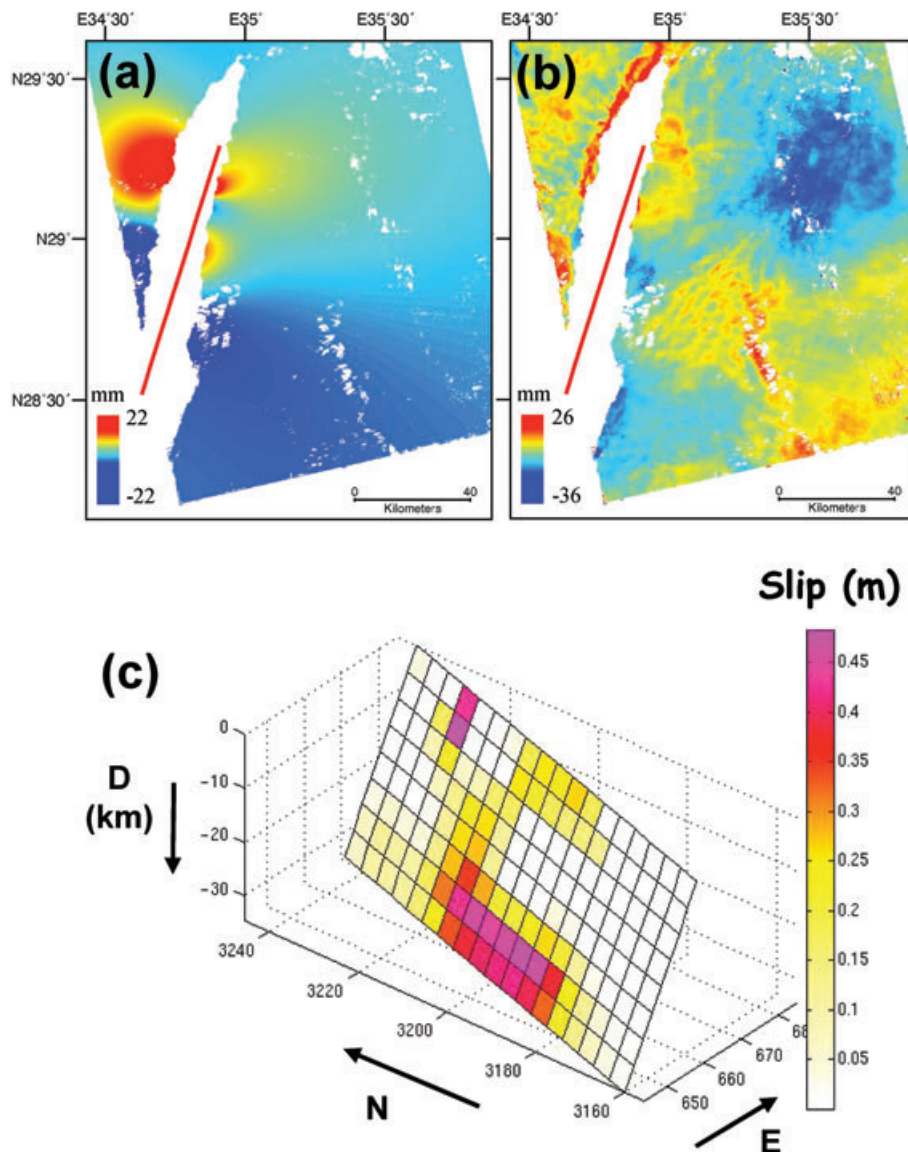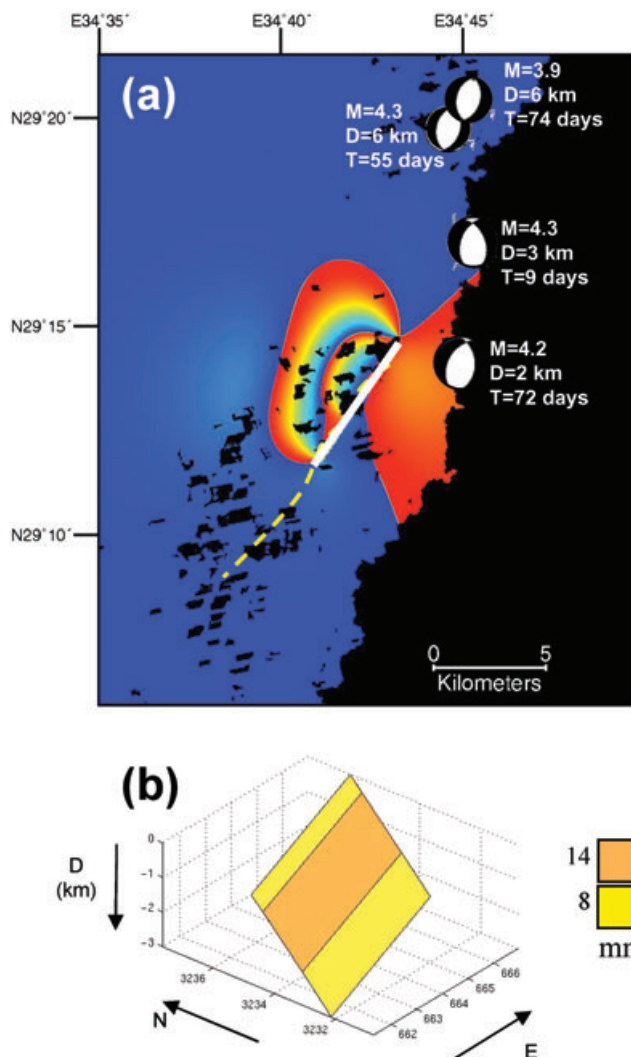
Figure 9. (a) Best-fitting ascending track model interferograms (synthetic) and (b) real-model residuals for the post-seismic deformation. (c) Slip distribution on the post-seismic fault model. See text for details. Fault location was determined by the coseismic inversion (Fig. 7).

Previous attempts to determine the fault parameters of the Nuweiba earthquake (Table 1) were based on seismological observations (Shamir 1996; Fattah *et al.* 1997; Pinar & Turkelli 1997; Klinger *et al.* 1999; Hofstetter *et al.* 2003), on InSAR (Baer *et al.* 1999, 2001; Klinger *et al.* 2000) and on integration of the two data types (Shamir *et al.* 2003). An analysis of the previous solutions with respect to the new interferograms is made for two of the previous models. First, we compare to the InSAR model of Baer *et al.* (1999), which is quite similar to the Klinger *et al.* (2000) model (Table 1). The model was generated by trial and error forward modelling and qualitative search for the best-fitting solution. In their best-fitting solutions the trade-offs between the slip and the width of the rupture plane are considerably high. The residual maps of their models show about four fringes on the western shores of the Gulf and three residual fringes on the eastern shores (Figs 12a and b). Next, we compare to the teleseismic waveform inversion of Hoffstetter *et al.* (2003), which solved for the moment release distribution along the fault. To make a synthetic interferogram of their
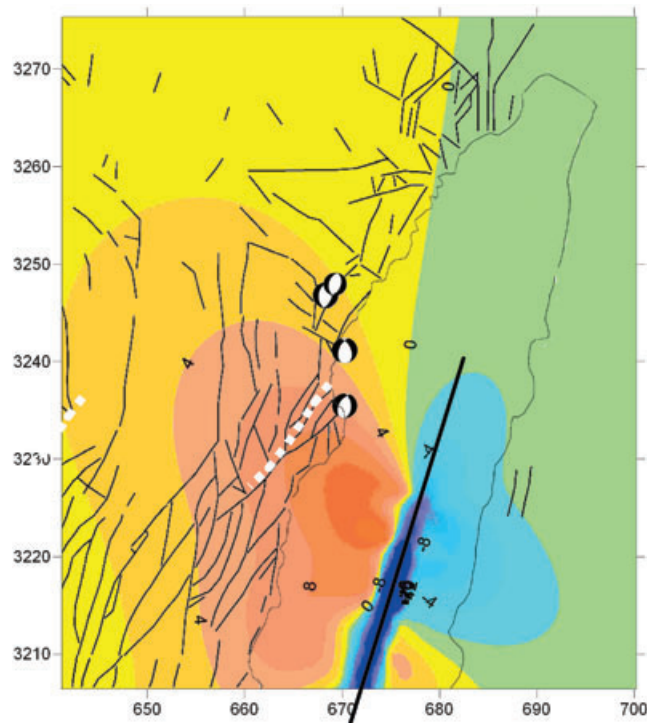
model we translated the moment distribution to slip distribution, using a published velocity and rigidity model for the crust in this region (Feigin & Shapira 1994). The residual map shows about 10 fringes on the eastern shores of the Gulf and about three residual fringes on the western shores (Figs 12c and d).

To explain these residuals we compare the fault parameters used in the above models to those of our inversion (Table 1). Parameters which do not differ significantly in the various models and are fairly well constrained, are the epicentre location, and the depth, strike, dip, rake and length of the fault. The total moment is also comparable in all models, and is slightly lower in the InSAR study of Baer *et al.* (1999). The major source of misfit between the present study and the model based on the teleseismic waveform inversion (Hofstetter *et al.* 2003) lies in the resolution of the slip distribution over the fault, and in particular the higher slip values and gradients and the smaller overall size of the rupture zone in the seismological model. We believe that the residuals and discrepancy could be further reduced by joint inversion of InSAR and seismological data.

Figure 11. Coulomb stress change (bars) induced by the Nuweiba earthquake in the area NW of the main rupture for normal faults dipping 60° to the NW, and striking 060°. White dashed line marks the location of the NE-striking lineament (Figs 5 and 6).

Figure 10. (a) Focal plane solutions of the 1 week to 6 months $M > 3.9$, $D < 6$ km aftershocks and model interferogram for the deformation NW of the main rupture. As model parameters we use the location and length of the NE lineament (Fig. 5) and the strike, dip and rake of the nearest aftershock. (b) Slip distribution along the fault computed by forward modelling.

Klinger *et al.* (1999) described gravitational collapses guided by pre-existing basement faults along the Gulf shorelines immediately following the main shock in which the eastern blocks were down-faulted. The post-seismic feature described above also follows a basement fault, and is also suggested to be triggered by the main shock, however, it does not seem to be of gravitational origin. First, it is located further inland from the Gulf shoreline and it is down-faulted westward (inland). Second, it occurred at least a week after

the main shock, and third, it seems to be associated with regional aftershock activity.

The cumulative moment production by all the aftershocks during the period of 17 months after the earthquake was about 1 per cent of the total coseismic moment release (7.7×10^{26} Dyn-cm; Hofstetter *et al.* 2003) and shows a logarithmic accumulation curve, punctuated by a few moderate ($5 < M < 6$) earthquakes (Fig. 13). At least 50 per cent of the total moment associated with these aftershocks was released during the first day after the main shock (without taking into account the incompleteness of the catalogue for that day), and over 95 per cent in the first 3 months (Fig. 13). The total (geodetic) moment released during the period 6–17 months after the Nuweiba earthquake is on the order of 15 per cent of the main shock moment. Comparing the coseismic deformation with the 1 week to 17 months deformation NW of the main rupture (Figs 4a and c) indicates that the moment released geodetically during the first 17 months after the earthquake is in the order of 25–30 per cent of the coseismic moment. This suggests that the crustal response to the Nuweiba earthquake by aftershocks is minor and secondary

Table 2. Aftershocks ($M > 3.9$; $D < 6$ km) NW of the rupture termination during the period of 1 week to 6 months after the main shock (Hofstetter *et al.* 2003).

| References[a]	Date[b]	Days[c]	Lat	Lon	Depth (km)	Strike	Dip	Rake	Mo (Dyn-cm)	M_w
29	951201	9	29.29	34.75	3	200;337	50;49	−59; −121	3.12e + 22	4.3
48	960116	55	29.34	34.73	6	8;188	46;44	−90; −90	2.75e + 22	4.3
50	960202	72	29.24	34.75	2	209;357	49;46	−68; −114	2.16e + 22	4.2
52	960204	74	29.35	34.74	6	14;192	46;44	−89; −91	7.31e + 21	3.9

[a]Reference number of aftershock from Hofstetter *et al.* (2003).
[b]yymmdd.
[c]Days after main shock.
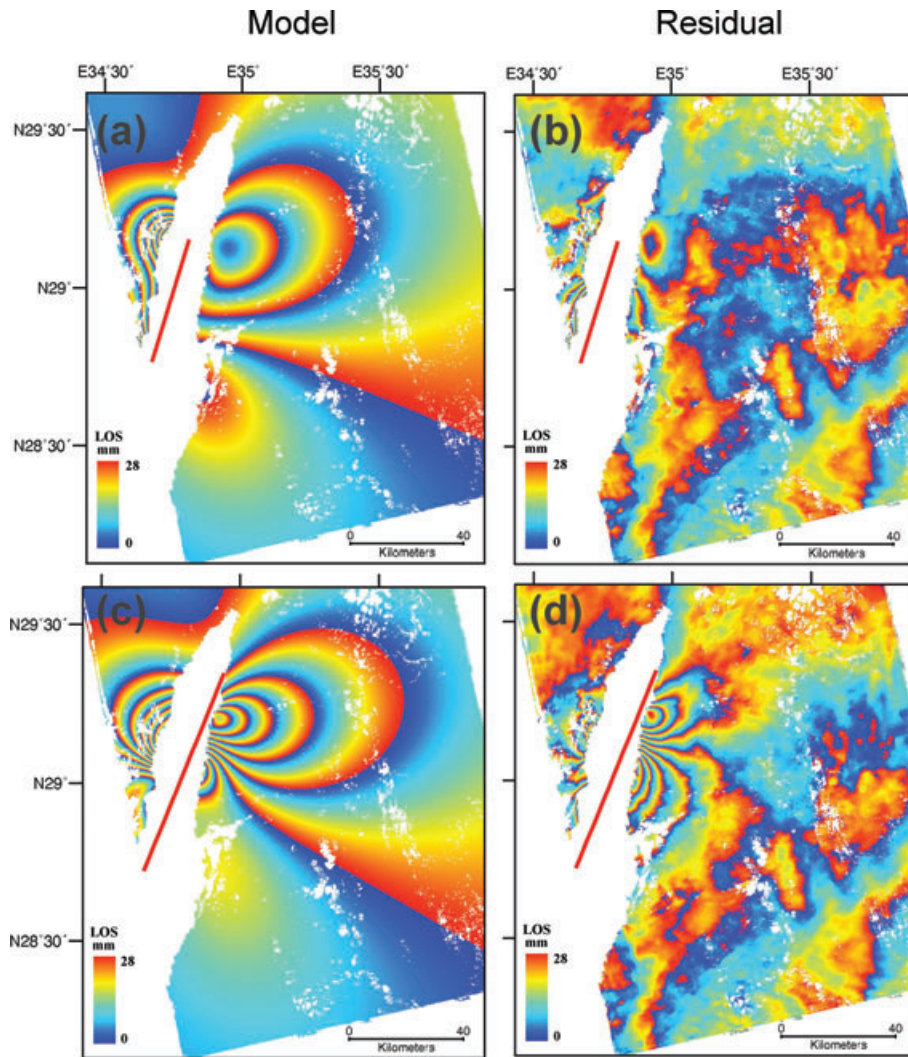
Figure 12. Previous model interferograms and their residuals from the coseismic interferograms of the present study. (a) and (b) Baer *et al.* 1999; (c) and (d) Hofstetter *et al.* (2003).
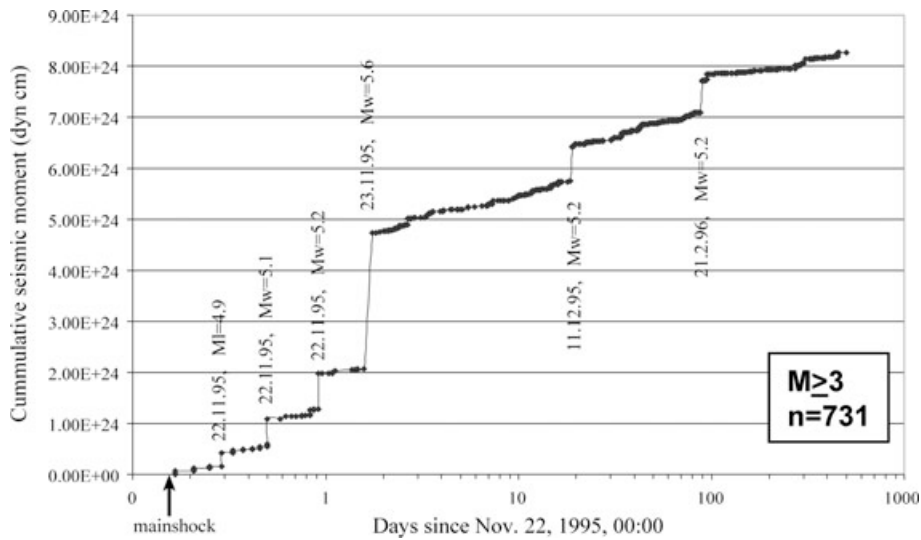
Figure 13. Cumulative seismic moment released in the 17 months following the Nuweiba earthquake for a region of 80 km × 150 km around the earthquake rupture to a depth of 30 km (GII 2006).

compared to aseismic creep, as previously noted for many other large earthquakes (e.g. Scholz 1972).

ACKNOWLEDGMENTS

REFERENCES

Amelung, F. & Bell, J. W., 2003. Interferometric synthetic aperture radar observations of the 1994 Double Spring Flat, Nevada, earthquake (M 5.9): main shock accompanied by triggered slip on a conjugate fault, *J. geophys. Res.,* **108**(B9), 2433, doi:10.1029/2002JB001953.

Baer, G., Sandwell, D., Williams, S., Bock Y. & Shamir, G., 1999. Coseismic deformation associated with the November 1995 Mw = 7.1 Nuweiba earthquake, Gulf of Elat/Aqaba, detected by synthetic aperture radar interferometry, *J. geophys. Res.,* **104,** 25 221–25 232.

Baer, G., Shamir, G., Sandwell, D. & Bock, Y., 2001. Crustal deformation during 6 years spanning the Mw = 7.2 1995 Nuweiba earthquake, analyzed by Interferometric Synthetic Aperture Radar, *Isr. J. Earth Sci.,* **50,** 9–22.

Bartov, Y., Eyal, M., Shimron, A.E. & Bentor, Y.K., 1980. *Sinai—Geological photomap 1:500, 000.* Survey of Israel.

Ben-Avraham, Z., 1985. Structural framework of the Gulf of Elat/Aqaba, *J. geophys. Res.,* **90,** 703–726.

Bodin, P., Bilham, R., Behr, J., Gomberg, J. & Hudnut, K. W., 1994. Slip triggered on southern California faults by the 1992 Joshua Tree, Landers and Big Bear earthquakes, *Bull. seism. Soc. Am.,* **84,** 806–816.

Bro, R. & De Jong, S., 1997. A fast non-negativity-constrained least squares algorithm, *J. Chemometrics,* **11,** 392–401.

Bürgmann, R., Rosen, P. & Fielding, E., 2000. Synthetic Aperture Radar interferometry to measure Earth's surface topography and its deformation, *Annu. Rev. Earth. planet. Sci.,* **28,** 169–209.

Clarke, P., Paradissis, D., Briole, P., England, P., Parsons, B., Billiris, H., Veis, G. & Ruegg, J.-C., 1997. Geodetic investigation of the 13 May 1995 Kozani-Grevena (Greece) earthquake, *Geophys. Res. Lett.,* **24,** 707–710.

Farr, T. & Kobrick, M., 2000. Shuttle Radar Topography Mission produces a wealth of data, *EOS Trans. AGU,* **81,** 583–585.

Fattah, A. K., Hussein, H. M., Ibrahim, E. M. & Atta, A. S. A. E., 1997. Fault plane solutions of the 1993 and 1995 Gulf of Aqaba earthquakes and their tectonic implications, *Annali di Geofisica,* **40,** 1555–1564.

Feigin, G. & Shapira, A., 1994. A unified crustal model for calculating travel times of seismic waves across the Israel Seismic Network, *IPRG,* Rep. Z1/567/79(107).

Fialko, Y., Sandwell, D., Agnew, D., Simons, M., Shearer, P. & Minster, B. 2002. Deformation on nearby faults induced by the 1999 Hector Mine earthquake, *Science,* **297,** 1858–1862.

Finzi, Y., 2005. Current deformation in the southern Dead Sea Transform: radar interferometry measurements and their tectonic implications, *Geological Survey of Israel report, GSI/24/04,* 74 p.

Funning, G. J., 2005. Source parameters of large shallow earthquakes in the Alpine-Himalayan belt from InSAR and waveform modeling, PhD thesis, University of Oxford, UK, 302 p.

Funning, G. J., Parsons, B., Wright, T. J., Jackson, J.A. & Fielding, E. J., 2005. Surface displacements and source parameters of the 2003 Bam (Iran) earthquake from Envisat advanced synthetic aperture radar imagery, *J. geophys. Res.,* **110,** B09406.

Gabriel, A.K., Goldstein, R.M. & Zebker, H.A., 1989. Mapping small elevation changes over large areas: differential Radar Interferometry, *J. geophys. Res.,* **94,** 9183–9191.

GII. 2006. Earthquakes in and around Israel, 1900–2006, Geophysical Institute of Israel.

Goldstein, R. M., Zebker, H. A., Werner, C. L., 1988. Satellite radar interferometry—two-dimensional phase unwrapping, *Radio Sci.,* **23,** 713–720.

Hanssen, R.F., 2001. *Radar Interferometry: Data Interpretation and Error Analysis,* Kluwer Academic Publishers, Dordrecht, The Netherlands, 308 p.

Hofstetter, A., Thio, H. K. & Shamir, G., 2003. Source mechanism of the 22/11/95 Gulf of Aqaba Earthquake and its aftershock sequence, *J. Seism.,* **7,** 99–114.

Joffe, S. & Garfunkel, Z., 1987. Plate kinematics of the circum Red Sea—a re-evaluation, *Tectonophysics,* **141,** 5–22.

Jónsson, S., Zebker, H., Segall, P. & Amelung, F., 2002. Fault slip distribution of the 1999 Mw 7.1 Hector Mine earthquake, California, estimated from satellite radar and GPS measurements. *Bull. seism. Soc. Am.,* **92**(4), 1377–1389.

Kikuchi, M., 1995. Teleseismic analysis of the Gulf of Aqaba, Egypt, earthquake of Nov. 22, 1995, YCU (Yokohama City University), Seismology Report No. 49.

King, G.C.P., Stein, R.S. & Lin, J., 1994. Static stress changes and the triggering of earthquakes, *Bull. seism. Soc. Am.,* **84,** 935–953.

King, G.C.P. & Bowman, D.D., 2003. The evolution of regional seismicity between large earthquakes, *J. geophys. Res.,* **108**(B2), 2096, doi:10.1029/2001JB000783.

Klinger, Y., Rivera, L., Haessler, H. & Maurin, J.-C., 1999. Active faulting in the Gulf of Aqaba: new knowledge from the Mw 7.3 earthquake of 22 November 1995, *Bull. seism. Soc. Am.,* **89,** 1025–1036.

Klinger, Y., Michel, R. & Avouac, J.-P., 2000. Coseismic deformation during the Mw7.3 Aqaba earthquake (1995) from ERS-SAR interferometry, *Geophys. Res. Lett.,* **27,** 3651–3654.

Massonnet, D. & Feigl, K.L., 1998. Radar interferometry and its applications to changes in the Earth's surface, *Rev. Geophys.,* **36,** 441–500.

Menke, W., 1989. *Geophysical Data Analysis: Discrete Inverse Theory,* Academic Press, San Diego.

Okada, Y., 1985. Surface deformation due to shear and tensile faults in a half space, *Bull. seism. Soc. Am.,* **75,** 1135–1154.

Pinar, A. & Turkelli, N., 1997. Source inversion of the 1993 and 1995 Gulf of Aqaba earthquakes, *Tectonophysics,* **283,** 279–288.

Price, E.J. & Sandwell, D.T., 1998. Small-scale deformation associated with the 1992 Landers, California earthquake mapped by synthetic aperture radar interferometry phase gradients, *J. geophys. Res.,* **103,** 27 001–27 016.

Press, W.H., Teokolsky, S.A., Vetterling, W.T. & Flannery, B.P., 1992. *Numerical Recipes in C: The Art of Scientific Computing,* 2nd edn, Cambridge University Press, Cambridge.

Rosen, P.A., Hensley, S., Joughin, I.R., Li, F.K., Madsen, S.N., Rodriguez, E. & Goldstein, R.M., 2000. Synthetic aperture radar interferometry, *Proc. IEEE,* **88**(3), 333–382.

Rosen, P.A., Hensley, S., Peltzer, G. & Simons, M., 2004. Updated repeat orbit interferometry package released, *EOS Trans. AGU,* **85**(5), 35.

Sarti, Y., Arkin, Y., Chorowicz, J., Karnieli, A. & Cunha, T., 2003. Assessing pre- and post-deformation in the southern Arava Valley segment of the Dead Sea Transform, Israel by differential interferometry, *Remote Sens. Environ.,* **86,** 141–149.

Scholz, C., 1972. Crustal movements in tectonic areas, *Tectonophysics,* **14,** 201–217.

Shamir, G., 1996. The November 22, 1995, Nuweiba earthquake, Gulf of Elat/Aqaba: mechanical analysis, The Geophysical Institute of Israel, Rep. 550/87/96(114).

Shamir, G., Baer G. & Hofstetter, A., 2003. Three-dimensional elastic earthquake modeling based on integrated seismological and InSAR data: the M_w = 7.2 Nuweiba earthquake, Gulf of Elat/Aqaba, 1995 November, *Geophys. J. Int.,* **154,** 731–744.

Stein, R., 1999. The role of stress transfer in earthquake occurrence, *Nature,* **402,** 605–609.

Toda, S. & Stein, R.S., 2002. Response of the San Andreas fault to the 1983 Coalinga-Nuñez Earthquakes: an application of interaction-based probabilities for Parkfield, *J. geophys. Res.,* **107,** doi:10.1029/2001JB000172.

Toda, S., Stein, R.S., Reasenberg, P.A. & Dietrich, J.H., 1998. Stress transferred by the $M_W = 6.5$ Kobe, Japan, shock: effect on aftershocks and future earthquake probabilities, *J. geophys. Res.,* **103,** 24 543–24 565.

Wright, T. J., Parsons, B., Jackson, J., Haynes, M., Fielding, E., England, P. & Clarke, P., 1999. Source parameters of the 1 October 1995 Dinar (Turkey) earthquake from SAR interferometry and seismic bodywave modeling, *Earth planet. Sci. Lett.,* **172,** 23–37.

Wright, T.J., Fielding, E.J. & Parsons, B.P., 2001. Triggered slip: observations of the 17 August 1999 Izmit (Turkey) earthquake using radar interferometry, *Geophys. Res. Lett.,* **25,** 1079–1083.

Wright, T.J., Lu, Z. & Wicks, C., 2003. Source model for the Mw 6.7, 23 October 2002 Nenana Mountain Earthquake (Alaska) from InSAR, *Geophys. Res. Lett.,* **30**(18), 1974, doi:10.1029/2003GL018014.